ACS APPLIED MATERIALS & INTERFACES

Research Article

www.acsami.org

# Three-Dimensional Expanded Graphene–Metal Oxide Film via Solid-State Microwave Irradiation for Aqueous Asymmetric Supercapacitors

MinHo Yang,[†,‡] Kyoung G. Lee,[‡] Seok Jae Lee,[‡] Sang Bok Lee,[*,†,§] Young-Kyu Han,[*,∥] and Bong Gill Choi[*,⊥]

[†]Graduate School of Nanoscience and Technology, Korea Advanced Institute of Science and Technology, Daejeon 305-701, Republic of Korea

[‡]Department of Nano Bio Research, National NanoFab Center (NNFC), Daejeon 305-806, Republic of Korea

[§]Department of Chemistry and Biochemistry, University of Maryland, College Park, Maryland 20742, United States

[∥]Department of Energy and Materials Engineering, Dongguk University—Seoul, Seoul 100-715, Republic of Korea

[⊥]Department of Chemical Engineering, Kangwon National University, Samcheok 245-711, Republic of Korea

Supporting Information

**ABSTRACT:** Carbon-based electrochemical double-layer capacitors and pseudocapacitors, consisting of a symmetric configuration of electrodes, can deliver much higher power densities than batteries, but they suffer from low energy densities. Herein, we report the development of high energy and power density supercapacitors using an asymmetric configuration of $Fe_2O_3$ and $MnO_2$ nanoparticles incorporated into 3D macroporous graphene film electrodes that can be operated in a safe and low-cost aqueous electrolyte. The gap in working potential windows of $Fe_2O_3$ and $MnO_2$ enables the stable expansion of the cell voltage up to 1.8 V, which is responsible for the high energy density (41.7 Wh $kg^{-1}$). We employ a household microwave oven to simultaneously create conductivity, porosity, and the deposition of metal oxides on graphene films toward 3D hybrid architectures, which lead to a high power density (13.5 kW $kg^{-1}$). Such high energy and power densities are maintained for over 5000 cycles, even during cycling at a high current density of 16.9 A $g^{-1}$.

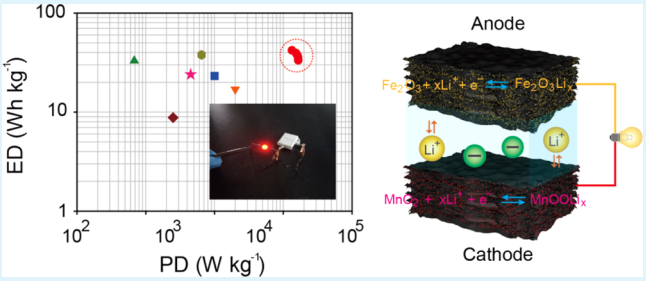


**KEYWORDS:** *hybrid film, graphene, metal oxide, microwave, supercapacitor*

## INTRODUCTION

Electrochemical energy storage devices such as secondary batteries and supercapacitors have recently gained popularity as effective power supplies in a number of applications from portable electronic devices, such as cell phones and laptops, to hybrid electric vehicles.[1] When compared with batteries, supercapacitors exhibit a much higher power density and a superior cycle life but exhibit an energy density ($E$) at least 1 order of magnitude lower than that of conventional batteries.[2] To meet the demands for future emerging markets, particularly sustainable road transport, supercapacitors should be designed to consist of safe, powerful electrochemical devices based on the high charge storage capacitance ($C$) of low-cost electrode materials combined with a large cell voltage ($V$), as indicated by the following equation: $E = 1/2CV^2$.[2] The capacitance and voltage depend strongly on the electrode materials, and they can be optimized by selecting suitable electrodes.[3] Hydrous $RuO_2$ is a state-of-the-art pseudocapacitive material capable of delivering a high specific capacitance of ~700 F $g^{-1}$ (in aqueous electrolytes),[4] which exceeds that of carbon materials that use double-layer charge storage.[2] However, the high cost and toxic nature of $RuO_2$ and voltage-limited aqueous electrolytes (<1.2 V) have limited their commercial applications. A large voltage window can be achieved at up to ~3.0 V using organic electrolytes based on aprotic solvents such as acetonitrile and propylene carbonate, but such a system is commonly employed for activated carbon-based supercapacitors with lower capacitances.[3,5] In addition, when compared to aqueous electrolytes, organic electrolytes suffer from high cost, lower ionic conductivity, and safety issues.[6]

One of the most attractive strategies to combine high energy and power densities within a single cell is to build hybrid supercapacitors, including composite electrode-based supercapacitors, battery-type supercapacitors, and asymmetric supercapacitors (ASCs).[6,7] Aqueous ASCs are of particular interest to efficient electrochemical storage, owing to their ability to

Received: July 9, 2015
Accepted: September 19, 2015
Published: September 19, 2015





DOI: 10.1021/acsami.5b06187
ACS Appl. Mater. Interfaces 2015, 7, 22364–22371

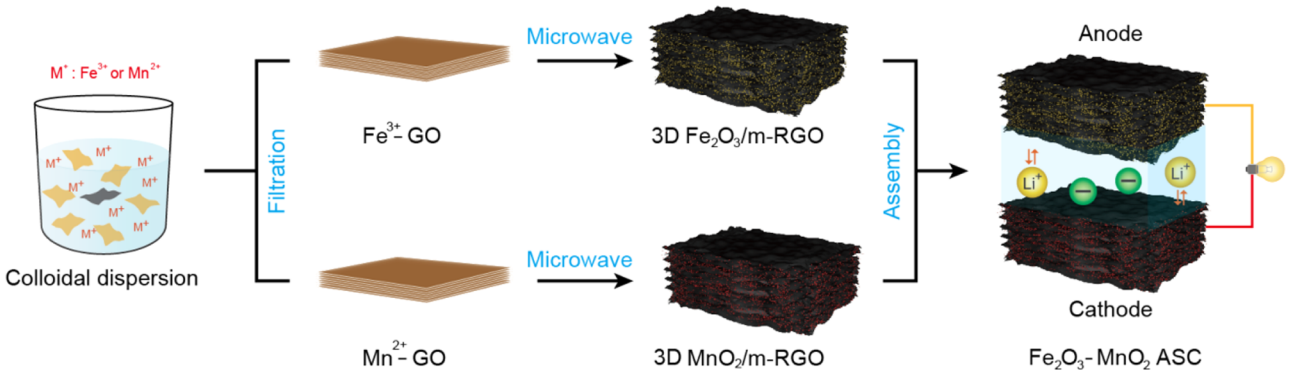


**Figure 1.** Schematic illustration of an experimental procedure for the preparation of 3D expanded hybrid structure films and an aqueous $Fe_2O_3$–$MnO_2$ ASC device.

improve energy density and the benefits of having an aqueous electrolyte, such as low cost, high safety, and environmental friendliness when compared to organic electrolytes.[7] A suitable combination of a negative electrode with high hydrogen evolution overpotential and a positive electrode with high oxygen evolution overpotential in the same cell enables the operating voltage window to be increased up to 2 V.[8] To date, intensive efforts have been devoted to exploring aqueous ASCs, such as $CoMoO_4$/graphene//activated carbon,[9] CoO@polypyrrole//activated carbon,[10] $MnO_2$//graphene,[11] and Ni$(OH)_2$/UGF//a-MEGO.[12] On the basis of the electrochemistry of active materials, iron–manganese (Fe–Mn) ASCs in aqueous electrolytes have great potential for high performance in electrochemical energy storage devices.[6,13,14] The integration of a negative electrode of $Fe_2O_3$ (from −1.0 to 0.0 V vs SCE) and a positive electrode of $MnO_2$ (from 0.0 to +1.0 V vs SCE) into a typical Fe–Mn ASC operating in safe aqueous electrolytes is capable of delivering a large voltage window of up to 2 V, which results in a high energy density (24 Wh $kg^{-1}$).[15] The utilization of both Fe and Mn realizes the further advantages of their low cost, natural abundance, and environmentally friendly nature. However, Fe–Mn ASCs undergo capacitance fading at high rates or during long-term cycling, primarily as a result of poor ionic and electronic transport in transition metal oxides.

The incorporation of pseudocapacitive oxide materials into a three-dimensional (3D) conductive architecture has been suggested to address the limitations of ionic and electronic transport kinetics in the design of electrodes.[3,9] In this respect, 3D graphene materials have been attracting intensive interest in this respect, owing to their intrinsic properties of 2D graphene sheets, guaranteed mass transport, relatively well-known surface chemistry for depositing guest nanoparticles (NPs), and ability to improve charge storage.[5,12,16] In particular, a free-standing form of 3D graphene electrodes could eliminate binders, additive carbons, and current collectors, which are essential to conventional supercapacitors, thereby improving gravimetric energy and power densities through lightweight electrodes.[16] To date, various approaches to developing 3D graphene have been attempted, including self-assembly in solution (e.g., hydrogels and aerogels)[17,18] and template-assisted growth (e.g., graphene sponges and films).[19,20] However, most of these methods are time-consuming and complicated experimental processes using high pressure or temperatures. The solid-state microwave irradiation offers a number of advantages over other solution-based process, such as enhanced product yield, energy- and time-saving process, and reduction in manufacturing cost.[21] Hence, the microwave-assisted methods have been employed to induce scalable production of expanded and reduced graphene oxide (RGO) materials and their composites including metal and metal oxide nanoparticles.[22−28]

However, to the best of our knowledge, no reports have yet appeared on the 3D porous and conductive RGO/metal oxide hybrid films based on the microwave-assisted method for energy storage applications.

Herein, we report a simple, rapid, and efficient strategy for the fabrication of 3D hybrid structured films using a familiar household microwave oven. Initially, we prepared metal ion (i.e., $Fe^{3+}$ or $Mn^{2+}$) incorporated GO films by vacuum filtration, which is widely used for making large areal mass and free-standing films. Microwave irradiation was then applied to convert metal ions/GO films into highly conductive and porous 3D hybrid films within 10 s, in which metal oxide NPs ($Fe_2O_3$ and $MnO_2$) were grown on the surface of microwave-treated RGO (3D m-RGO). As-prepared 3D $Fe_2O_3$/m-RGO and 3D $MnO_2$/m-RGO films were employed as the anode and cathode, respectively, to build aqueous $Fe_2O_3$–$MnO_2$ ASC devices (Figure 1). In this cell configuration, the 3D m-RGO films were efficient and convenient current collectors for accepting charges (electrons and ions) and for removing binders, additive carbons, and conventional metal current collectors. As a result, our ASCs based on such 3D hybrid film electrodes deliver high energy density over long-term cycling of 5000 cycles while maintaining high power density.

## EXPERIMENTAL SECTION

**Preparation of 3D $Fe_2O_3$/ and $MnO_2$/m-RGO Films.** The starting material was water-dispersed GOs synthesized by the modified Hummer's method.[29] For microwave-assisted solid-state reactions, 5 wt % of RGO as a microwave susceptor was added to 95 wt % of a GO suspension and then uniformly dispersed by sonication for 1 h. The 3D $Fe_2O_3$/m-RGO films were prepared as follows: first, 20 mg of GO/RGO was dispersed in 20 mL of isopropyl alcohol–water (1:1 v/v) solution by sonication for 1 h, after which 5 mM $FeCl_3$ was slowly added to the GO/RGO dispersion to form a stable suspension. Subsequently, the mixture of GO/RGO and $FeCl_3$ was stirred for 30 min, and it was filtered using an AAO membrane. The free-standing $Fe^{3+}$-incorporated GO/RGO films were peeled from the AAO membrane and treated by microwave irradiation for 10 s. The 5 mM manganese acetate was subsequently used for the preparation of the 3D $MnO_2$/m-RGO films through the same protocol used for the 3D $Fe_2O_3$/m-RGO films. For comparison, the 3D m-RGO and RGO films were prepared by microwave irradiation and by hydrazine treatment of GO at 85 °C, respectively.

**Characterization of Materials and Electrochemical Measurements.** Scanning electron microscopy (SEM) images were obtained


DOI: 10.1021/acsami.5b06187
ACS Appl. Mater. Interfaces 2015, 7, 22364−22371

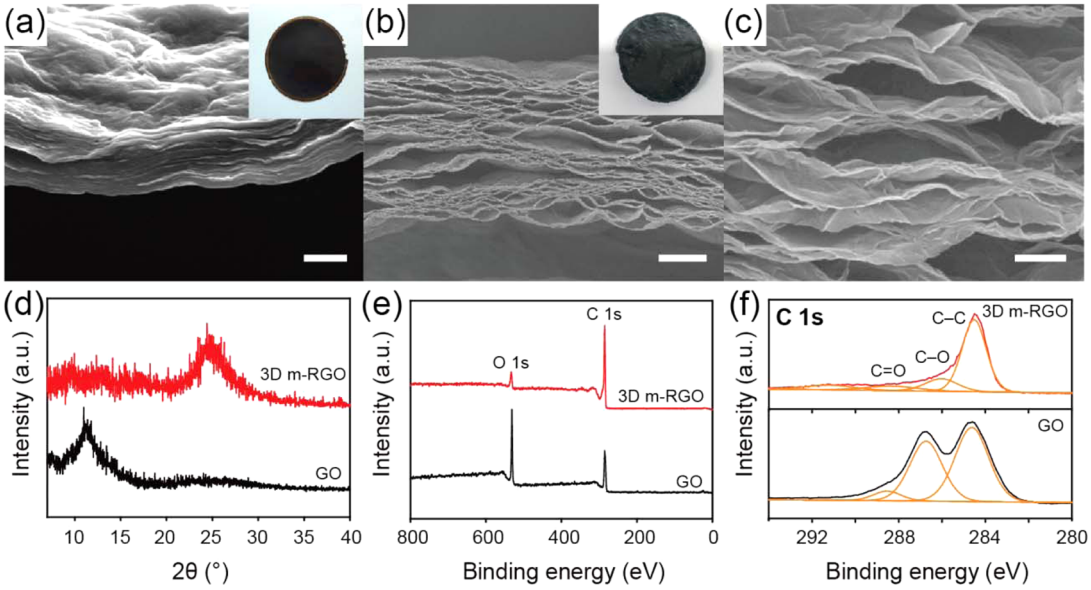


**Figure 2.** Cross-section SEM images of (a) GO film and (b,c) 3D m-RGO film at low and high magnification, respectively. (Insets) Digital-photo images of the free-standing GO and 3D m-RGO films. (d) XRD patterns of GO and m-RGO films. (e) Survey XPS spectra and (f) C 1s core level XPS spectra of GO and 3D m-RGO films. Scale bars: 1 (a, c) and 20 $\mu$m (b).

using a field emission scanning electron microscope (S-4800). X-ray diffraction (XRD) data were obtained on a Rigaku D/max IIIC (3 kW) with a $q/q$ goniometer equipped with a Cu K$\alpha$ radiation generator. X-ray photoelectron spectroscopy (XPS) data were obtained using a Thermo MultiLab 2000 system. High-resolution transmission electron microscopy (HRTEM) images were obtained using a field-emission TEM (JEM2100F, JEOL Ltd.) operated at 200 kV. Thermogravimetric analysis (TGA) was conducted using a TGA 92-18 (Setaram) with a heating rate of 10 °C min$^{-1}$. Cyclic voltammetry (CV), galvanostatic charge/discharge measurements, electrochemical impedance spectroscopy (EIS, from $10^5$ to $10^{-2}$ Hz with 10 mV amplitude), and cycling performance were evaluated using a VersaSTAT 4 (Princeton Applied Research). For electrochemical tests, the RGO, 3D m-RGO, 3D $Fe_2O_3$, and $MnO_2$/m-RGO films were used directly as working electrodes without the addition of any conducting agent or binder. The electrical connection was accomplished by bonding aluminum tabs onto the edge of free-standing films with silver paste. In a three-electrode system, Pt wire and Ag/AgCl were used as the counter and reference electrodes, respectively. The aqueous ASCs with 3D $Fe_2O_3$/m-RGO as a negative electrode and 3D $MnO_2$/m-RGO film as a positive electrode were evaluated in a two-electrode configuration.

**Calculations.** The specific capacitance of each electrode in the three-electrode configuration was calculated from the CV curves at various scan rates using the following equation[17]

$$C = \frac{1}{2mv\Delta V}\int i\,dV$$

where $i$ is the current (A), $\int i\,dV$ is the integration area for the CV curves, $v$ is the scan rate (V s$^{-1}$), $m$ is the mass (g) of the electrode, and $\Delta V$ is the potential window (V).

To assemble ASCs, the loading mass ratio was estimated as follows[6]

$$\frac{m^-}{m^+} = \frac{C^+ \times \Delta V^+}{C^- \times \Delta V^-}$$

where $m^-$ and $m^+$, $C^-$ and $C^+$, and $\Delta V^-$ and $\Delta V^+$ are the mass (g), specific capacitance (F g$^{-1}$) from CV curves, and potential widows (V) of the three-electrode configuration of the individual negative and positive electrodes, respectively.

The specific capacitance of aqueous ASCs in the two-electrode configuration was calculated from galvanostatic charge/discharge curves based on the following equation[3]

$$C = \frac{I\Delta t}{m\Delta V}$$

where $I$ is the discharge current, $\Delta t$ is the time for a full discharge, $m$ is the total mass of the electrode without current collector, and $\Delta V$ represents the change in voltage during the discharge process.

The energy and power densities of ASCs derived from galvanostatic charge/discharge curves were calculated using the following equations[12]

$$E = \frac{1}{2}C(V_{max})^2$$

$$P = \frac{(V_{max} - V_{drop})^2}{4RM}$$

where $C$ is the specific capacitance, $V_{max}$ is the cell voltage, $R$ is the internal resistance from the $IR$ drop (= $V_{drop}/2I$), and $M$ is the total weight of both electrodes without current collectors.

## RESULTS AND DISCUSSION

In this study, we adopted solid-state microwave methods to allow simultaneously for reduction, porous structure, and metal oxide deposition on a packed, layered GO film using a microwave oven. The microwave irradiation could not only directly reduce GOs into RGOs but also efficiently prevent the restacking of individual RGO sheets through the generation of volatile gaseous species (i.e., $H_2O$, CO, and $CO_2$) generated by the decomposition of oxygen-containing functional groups.[24,25] The preparation of porous structured RGO films was first attempted using a microwave oven. In this process, free-standing GO films were prepared by vacuum filtration of GO dispersed in water using a flow-directed assembly. We added presynthesized graphene materials (5 wt %) to GO dispersion as a microwave susceptor before filtration, which could be easily dispersed in water, to enable the effective reduction and expansion of the GO sheets.[25] Observation using SEM revealed compact layered structures of GO films with a thickness of 1.6 ± 0.16 $\mu$m (Figure 2a). Following microwave irradiation for 10 s, free-standing foam-like RGO films were obtained (Figure 2b). It should be noted that a longer irradiation time (>10 s)


DOI: 10.1021/acsami.5b06187
ACS Appl. Mater. Interfaces 2015, 7, 22364−22371

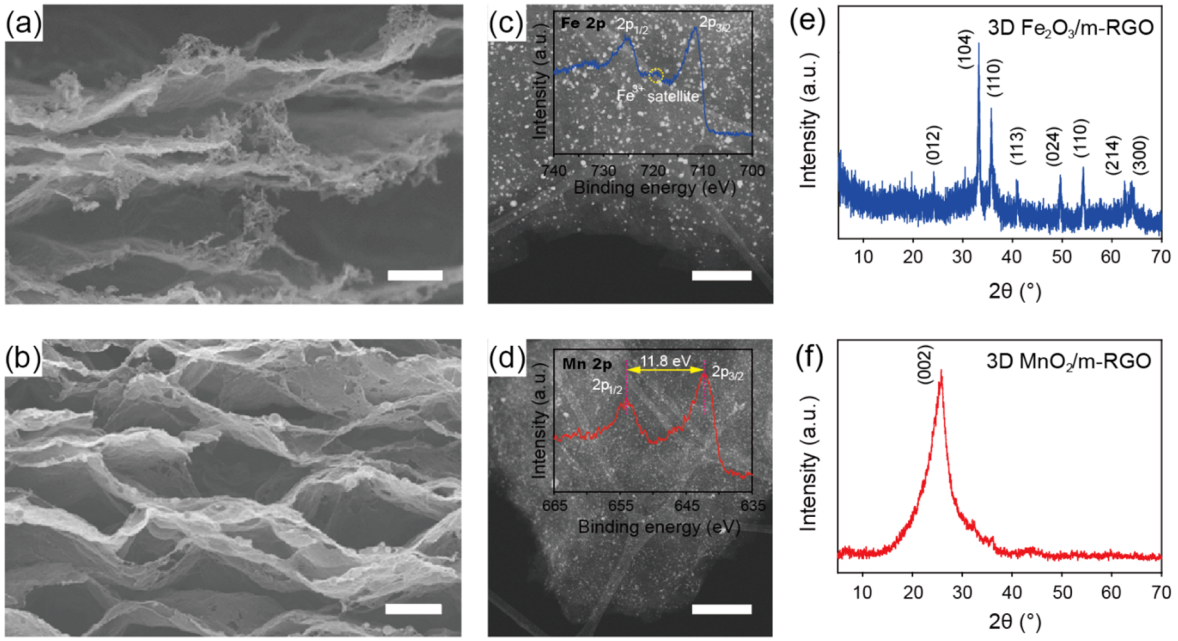


**Figure 3.** Top and bottom columns are corresponding cross-section SEM images, TEM images, and XRD patterns of (a, c, and e) 3D $Fe_2O_3$/m-RGO and (b, d, and f) 3D $MnO_2$/m-RGO films, respectively. (Insets) High-resolution XPS spectra of Fe 2p and Mn 2p for 3D $Fe_2O_3$/m-RGO and 3D $MnO_2$/m-RGO films, respectively. Scale bar: 1 $\mu$m (a), 20 $\mu$m (b), and 500 nm (c, d).

caused significant cracking and mass loss of the films, possibly due to arcing-induced ignition, which indicates that the irradiation time should be controlled within 10 s (Figure S1, Supporting Information). The 3D m-RGO films clearly had 3D porous network structures with a pore size of submicrometer to several micrometers, in which the RGO sheets were well separated (Figure 2b and 2c). The thickness of the 3D m-RGO was 61.6 ± 4.56 $\mu$m (Figure 1b), which is about 40 times greater than that of the original GO films. This volume of expansion was also observed in previously reported studies regarding the formation of gaseous species.[30] To demonstrate the successful reduction of GO sheets, changes in the peak positions and intensities in XRD and XPS measurements were investigated using GO and 3D m-RGO film samples (Figure 2d, 2e, and 2f). After microwave treatment, the 2$\theta$ peak (10.9°) of GO films disappeared, and then the characteristic graphene (002) peak was observed at 24.4° with an interlayer distance of 0.36 nm because of the deoxygenation reaction during microwave irradiation.[25] Upon analysis of the XPS spectra, the oxygen-related groups significantly decreased in 3D m-RGO films when compared with GO films. These results indicate that microwave irradiation enables the transformation of insulating GO films into conductive RGO films.

We also synthesized metal oxides of $Fe_2O_3$ and $MnO_2$ onto the surface of RGO sheets during microwave irradiation using metal precursor-incorporated GO films (Figure S2, Supporting Information). It is known that noble metals and metal oxide nanoparticles can be synthesized and deposited onto carbon surfaces using solvent-free microwave irradiation.[27,28] This successful deposition of nanoparticles completed a direct fabrication of highly conductive and porous 3D m-RGO hybrid films. A reduction reaction and exfoliation accompanied the deposition of metal oxides (Figure 3 and Figure S3, Supporting Information). A TEM analysis of the 3D $Fe_2O_3$ and $MnO_2$/m-RGO sheets showed that metal oxide NPs were uniformly distributed on the 3D m-RGO sheets (Figure S4, Supporting Information). The average TEM diameter was found to be 20 ± 5.1 nm for $Fe_2O_3$ and 22 ± 11.6 nm for $MnO_2$ (Figure 3c and 3d). To confirm the crystal structure of the metal oxides, XRD patterns of as-prepared hybrid films were measured. As shown in the XRD pattern of Figure 3e, all diffraction peaks could be assigned to the well-crystallized $Fe_2O_3$ with a rhombohedral phase (JCPDS No. 33-0664).[31] The XRD pattern of Figure 3f for the 3D $MnO_2$/m-RGO film only exhibited a broad and weak diffraction (002) graphene peak at 24.5°, indicating that $MnO_2$ had an amorphous structure.[20]

High-resolution XPS measurements were performed to investigate the chemical state of $Fe_2O_3$ and $MnO_2$ on 3D m-RGO films (Figure 3c and 3d, inset). The peak positions of the Fe $2p_{3/2}$ and Fe $2p_{1/2}$ spectra of the 3D $Fe_2O_3$/m-RGO films are located at 711.7 and 725.3 eV, respectively, which are characteristic peaks of $\alpha$-$Fe_2O_3$.[31] The spin energy separation between Mn $2p_{3/2}$ (641.8 eV) and Mn $2p_{1/2}$ (653.6 eV) was 11.8 eV, which was in accordance with the predominant peaks of $Mn^{4+}$.[11] The loading amount of metal oxides deposited on the RGO surface was quantified by the TGA measurements. From the results, 80 wt % of $Fe_2O_3$ and 65 wt % of $MnO_2$ were deposited on the surface of RGO (Figure S5, Supporting Information).

The electrochemical properties of as-prepared $Fe_2O_3$/m-RGO and $MnO_2$/m-RGO films were evaluated as positive and negative electrodes, respectively, using a three-electrode system. A portion of the 3D $Fe_2O_3$/m-RGO or 3D $MnO_2$/m-RGO film (1 × 1 $cm^2$) was dipped into 2 M LiCl aqueous solution with an Ag/AgCl reference electrode and a Pt wire counter electrode. To enable a better comparison, 3D m-RGO and 2D packed RGO (without microwave treatment) films were also tested under the same conditions. The CV of the 3D m-RGO film revealed a typical electrical double-layer capacitive behavior (Figure S6, Supporting Information). The specific capacitance of 3D m-RGO films was 205 F $g^{-1}$, which is two times higher than that of RGO films (98 F $g^{-1}$). These findings clearly demonstrate that the 3D porous structure improved the capacitance. Figure 4a shows the CV curves of 3D $Fe_2O_3$ and


DOI: 10.1021/acsami.5b06187
ACS Appl. Mater. Interfaces 2015, 7, 22364−22371

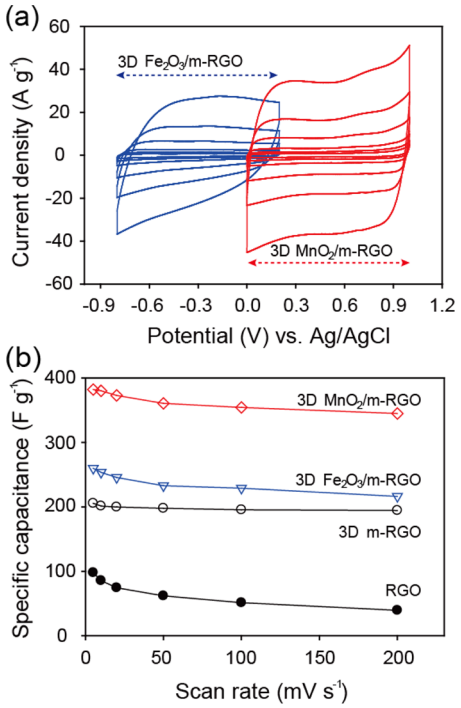


**Figure 4.** CVs of (a) 3D $Fe_2O_3$/m-RGO and (b) 3D $MnO_2$/m-RGO at various scan rates in 2 M LiCl. (b) Specific capacitances of RGO, 3D m-RGO, 3D $MnO_2$/m-RGO, and 3D $Fe_2O_3$/m-RGO for a comparison as a function of increasing the scan rate from 5 to 200 mV $s^{-1}$.

$MnO_2$/m-RGO films at various scan rates. All CV curves for 3D $Fe_2O_3$ and $MnO_2$/m-RGO showed semirectangular shapes. The related specific capacitances of those films were calculated and plotted in Figure 4b. At all scan rates, the 3D hybrid films showed continuously higher specific capacitances than the 3D m-RGO and RGO films, indicating that the capacitances of 3D hybrid films contributed to the combination of the electrical of metal oxides. At a scan rate of 5 mV $s^{-1}$, a maximum specific capacitance of 382 F $g^{-1}$ was obtained for the 3D $MnO_2$/m-RGO film, while that of the 3D $Fe_2O_3$/m-RGO film was 260 F $g^{-1}$. As the scan rate increased, the specific capacitances of the 3D hybrid films decreased slightly, with retention values of 83% and 90% observed for the 3D $Fe_2O_3$ and $MnO_2$/m-RGO films, respectively.

It is essential to demonstrate the origin of the superior electrochemical performance of 3D hybrid films compared to the 2D packed RGO films. EIS is a powerful method for the investigation of electron and ion transfer in supercapacitor electrodes.[32] As shown in the Nyquist plot (Figure 5a), the charge transfer resistances of the 3D hybrid films (8.7 and 8.2 Ω for 3D $Fe_2O_3$ and $MnO_2$/m-RGO, respectively) were much lower than those of packed, layered RGO films (17.3 Ω), even though these values were slightly higher than those of 3D m-RGO film (7.2 Ω). Moreover, the relaxation time constant ($\tau_0 = 1/f_0$), the minimum time to accumulate a charge on the electrode surface with an efficiency of greater than 50%,[33] was calculated to be 0.6 s for 3D m-RGO, 0.8 s for 3D $MnO_2$/m-RGO, and 1.0 s for 3D $Fe_2O_3$/m-RGO (Figure 5b and 5c). These values are much shorter than those of RGO films (7.9 s) and the reported carbon-based electrodes (2.5−14 s),[32,34,35] which demonstrate the high power performance of 3D m-RGO and hybrid films. This excellent power performance must be attributed to the well-defined interconnected 3D structures that serve as a highway for electron and ion transfers.[16]

The aqueous ASC configuration with free-standing 3D macroporous hybrid films is displayed in Figure 1. The ASC unit cell (3D $Fe_2O_3$/m-RGO//3D $MnO_2$/m-RGO) consisted of 3D $Fe_2O_3$ and $MnO_2$/m-RGO films as an anode and a cathode, respectively, with a safe aqueous 2 M LiCl as an

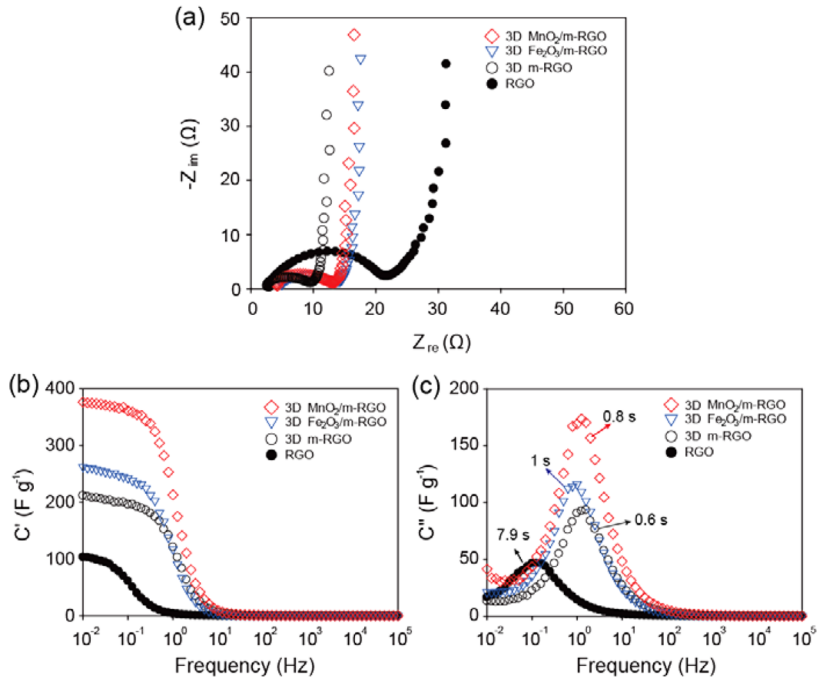


**Figure 5.** (a) Nyquist plot for 3D $MnO_2$/m-RGO, 3D $Fe_2O_3$/m-RGO, 3D m-RGO, and RGO films. Spectra were taken in 2 M LiCl in a frequency range from 100 kHz to 10 mHz. (b and c) Frequency dependence of the real and imaginary parts (C′ and C″) of the specific capacitance of four different electrodes.



DOI: 10.1021/acsami.5b06187
ACS Appl. Mater. Interfaces 2015, 7, 22364−22371

electrolyte. The stable potential window of 3D $Fe_2O_3$/m-RGO was between −0.8 and 0.2 V (vs Ag/AgCl), while 3D $MnO_2$/m-RGO was stably cycled between 0 and 1.0 V (vs Ag/AgCl) (Figure 4a). As expected, our ASC cells extended an operating cell voltage up to 1.8 V with a semirectangular shape of CVs (Figure 6a). This wide voltage window of ASC cells efficiently

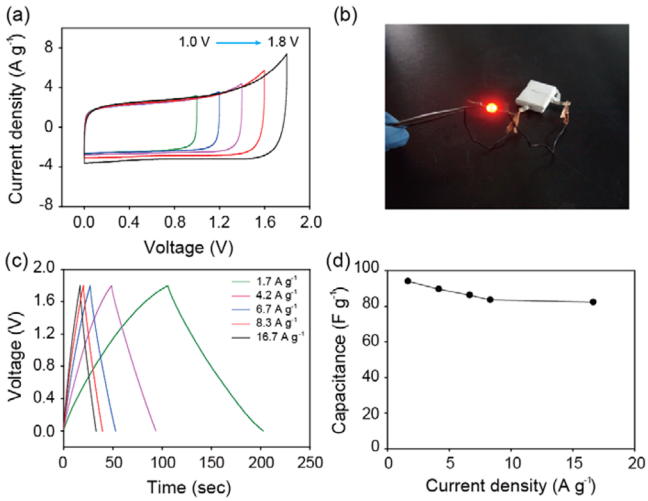


**Figure 6.** (a) CV curves of the assembled ASC devices (full-cell configuration) collected in different scan voltage windows at a scan rate of 20 mV $s^{-1}$. (b) Red LED lit by the ASC devices. (c) Galvanostatic charge/discharge curves of ASC devices at various current densities. (d) Plot of full-cell capacitance vs current density.

powered a commercial red light emitting diode (LED; 1.7 V, 30 mA, and 5 mm diameter) after being charged (Figure 6b). These results were attributed to not only a combination negative and positive the electrode materials that have well-separated potential windows but also utilization of nanocarbons that efficiently block oxygen or hydrogen evolution reaction.[8] The galvanostatic charge/discharge measurement was also tested using ASC cells at various current densities (Figure 6c). The gravimetric capacitances for our ASC full cells were calculated and plotted (Figure 6d). Even when the current densities were increased to 16.7 A $g^{-1}$, as-assembled ASCs maintained 88% capacitance retention relative to their initial value, implying a good rate capability. Notably, when cycled under harsh conditions (16.7 A $g^{-1}$), this value (73.9 F $g^{-1}$) was still higher than reported for other ASCs.[8,11,14,15] In addition, the 3D hybrid film-based ASCs had good durability for long-term cycling with 89% capacitance retention observed after 5000 cycles, even when cycling at a high current density of 16.9 A $g^{-1}$ (Figure S7, Supporting Information). An SEM study on 3D hybrid films after the cycling test was performed, which provided good evidence for the excellent cycle performance.[36−38] Despite the fact that the pore size was reduced during the assembly of ASCs, the 3D hybrid films still maintained a porous network morphology without any visible cracks, leading to superior cycle stability.

We evaluated energy ($E$) and power ($P$) densities of our ASC devices from the galvanostatic charge/discharge curves and plotted the corresponding specific $E$ versus $P$ values in a Ragone plot (Figure 7a). The maximum energy density was 41.7 Wh $kg^{-1}$ at a power density of 13.5 kW $kg^{-1}$, which was significantly improved compared to previously reported iron- and/or manganese-based ASCs, such as $Fe_3O_4$//$MnO_2$ (8.8

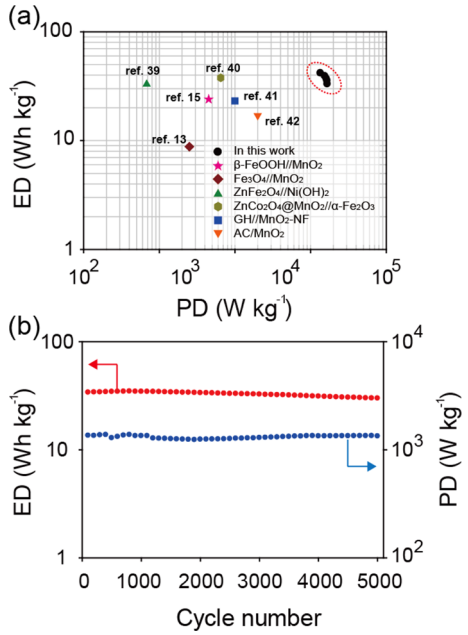


**Figure 7.** (a) Ragone plot of assembled ASCs (full-cell configuration) compared with other ASCs in an aqueous system. (b) Performance durability of assembled ASC devices measured at 16.7 A $g^{-1}$.

Wh $kg^{-1}$ at 0.25 kW $kg^{-1}$),[13] $\beta$-FeOOH//$MnO_2$ (24 Wh $kg^{-1}$ at 0.45 kW $kg^{-1}$),[15] $ZnFe_2O_4$//$Ni(OH)_2$ (33 Wh $kg^{-1}$ at 0.068 kW $kg^{-1}$),[39] $ZnCo_2O_4$@$MnO_2$//$\alpha$-$Fe_2O_3$ (37.8 Wh $kg^{-1}$ at 0.65 kW $kg^{-1}$),[40] GH//$MnO_2$−NF (23.2 Wh $kg^{-1}$ at 1.0 kW $kg^{-1}$),[41] and AC//$MnO_2$ (17 Wh $kg^{-1}$ at 2 kW $kg^{-1}$).[42] Notably, our ASC full cells maintained 88.2% energy retention and 98.7% power retention of their initial values after 5000 cycles (Figure 7b).

The superior performance of supercapacitors that assembled the asymmetric configuration of 3D $Fe_2O_3$ and $MnO_2$/m-RGO hybrid films is attributed to the unique 3D hybrid nanostructure and large potential gap between two electrodes. The pairing of two different hybrid electrodes surpassed the operative voltage limit in aqueous supercapacitors by employing high-overpotential hybrid materials for both hydrogen and oxygen evolution.[16] It extended the operating voltage up to 1.8 V of the assembled supercapacitors, contributing to improvement in energy density. In addition, highly conductive 3D networks formed by the solid-state microwave reaction enabled the enhanced kinetic behavior of ion and electron transport, leading to a high level of power density.

## CONCLUSIONS

We developed for the first time a rapid and simultaneous synthetic method for the fabrication of 3D porous and conductive hybrid films obtained directly from 2D packed GO-based films. A series of highly pseudocapacitive materials of $Fe_2O_3$ and $MnO_2$ was synthesized using this method, and it could be extended to a variety of other NP-deposited 3D hybrid materials for many electrochemical applications. Of note, the gap in the working potential windows in aqueous electrolytes between $Fe_2O_3$ and $MnO_2$ allowed us to design and build asymmetric $Fe_2O_3$−$MnO_2$ supercapacitors with a large potential window of 1.8 V that could combine high energy and power densities with a good cycling life. This asymmetric cell configuration based on 3D hybrid film electrodes could


DOI: 10.1021/acsami.5b06187
ACS Appl. Mater. Interfaces 2015, 7, 22364−22371

meet the demands for applications in powering consumer electronics and transportation.

## ■ ASSOCIATED CONTENT

### Supporting Information

The Supporting Information is available free of charge on the ACS Publications website at DOI: 10.1021/acsami.5b06187.

Photo, EDS mapping, XPS, TEM, TGA, and some electrochemical properties (PDF)

## ■ AUTHOR INFORMATION


### Corresponding Authors

*E-mail: slee@umd.edu.
*E-mail: ykenergy@dongguk.edu.
*E-mail: bgchoi@kangwan.ac.kr.


### Notes

The authors declare no competing financial interest.

## ■ ACKNOWLEDGMENTS

This work was supported by the National Research Foundation of Korea (NRF) grant funded by the Ministry of Science, ICT and Future Planning of Korea (No. 2014R1A5A2010008 and No. 2015R1C1A1A02036556), and the Research and Development Program of Korea Institute of Energy Research (B5-2414). This work was also supported by the Dongguk University Research Fund of 2013.

## ■ REFERENCES


(1) Hall, P. J.; Bain, E. J. Energy-Storage Technologies and Electricity Generation. *Energy Policy* **2008**, *36*, 4352−4355.

(2) Hall, P. J.; Mirzaeian, M.; Fletcher, S. I.; Sillars, F. B.; Rennie, A. J. R.; Shitta-Bey, G. O.; Wilson, G.; Cruden, A.; Carter, R. Energy Storage in Electrochemical Capacitors: Designing Functional Materials to Improve Performance. *Energy Environ. Sci.* **2010**, *3*, 1238−1251.

(3) Wang, G.; Zhang, L.; Zhang, J. A Review of Electrode Materials for Electrochemical Supercapacitors. *Chem. Soc. Rev.* **2012**, *41*, 797−828.

(4) Zheng, J. P.; Cygan, P. J.; Jow, T. R. Hydrous Ruthenium Oxide as an Electrode Material for Electrochemical Capacitors. *J. Electrochem. Soc.* **1995**, *142*, 2699−2703.

(5) Béguin, F.; Presser, V.; Balducci, A.; Frackowiak, E. Carbons and Electrolytes for Advanced Supercapacitors. *Adv. Mater.* **2014**, *26*, 2219−2251.

(6) Yan, J.; Wang, Q.; Wei, T.; Fan, Z. Recent Advances in Design and Fabrication of Electrochemical Supercapacitors with High Energy Densities. *Adv. Energy Mater.* **2014**, *4*, 1300816.

(7) Wang, F.; Xiao, S.; Hou, Y.; Hu, C.; Liu, L.; Wu, Y. Electrode Materials for Aqueous Asymmetric Supercapacitors. *RSC Adv.* **2013**, *3*, 13059−13084.

(8) Brousse, T.; Toupin, M.; Bélanger, D. A Hybrid Activated Carbon-Manganese Dioxide Capacitor Using a Mild Aqueous Electrolyte. *J. Electrochem. Soc.* **2004**, *151*, A614−A622.

(9) Yu, X.; Lu, B.; Xu, Z. Super Long-Life Supercapacitors Based on the Construction of Nanohoneycomb-Like Strongly Coupled $CoMoO_4$-3D Graphene Hybrid Electrodes. *Adv. Mater.* **2014**, *26*, 1044−1051.

(10) Zhou, C.; Zhang, Y.; Li, Y.; Liu, J. Construction of High-Capacitance 3D CoO@Polypyrrole Nanowire Array Electrode for Aqueous Asymmetric Supercapacitor. *Nano Lett.* **2013**, *13*, 2078−2085.

(11) Wu, Z.-S.; Ren, W.; Wang, D.-W.; Li, F.; Liu, B.; Cheng, H.-M. High-Energy $MnO_2$ Nanowire/Graphene and Graphene Asymmetric Electrochemical Capacitors. *ACS Nano* **2010**, *4*, 5835−5842.

(12) Ji, J.; Zhang, L. L.; Ji, H.; Li, Y.; Zhao, X.; Bai, X.; Fan, X.; Zhang, F.; Ruoff, R. S. Nanoporous $Ni(OH)_2$ Thin Film on 3D Ultrathin-Graphite Foam for Asymmetric Supercapacitor. *ACS Nano* **2013**, *7*, 6237−6243.

(13) Brousse, T.; Bélanger, D. A Hybrid $Fe_3O_4$-$MnO_2$ Capacitor in Mild Aqueous Electrolyte. *Electrochem. Solid-State Lett.* **2003**, *6*, A244−A248.

(14) Yang, P.; Ding, Y.; Lin, Z.; Chen, Z.; Li, Y.; Qiang, P.; Ebrahimi, M.; Mai, W.; Wong, C. P.; Wang, Z. L. Low-Cost High-Performance Solid-State Asymmetric Supercapacitors Based on $MnO_2$ Nanowires and $Fe_2O_3$ Nanotubes. *Nano Lett.* **2014**, *14*, 731−736.

(15) Jin, W.-H.; Cao, G.-T.; Sun, J.-Y. Hybrid Supercapacitor Based on $MnO_2$ and Columned FeOOH Using $Li_2SO_4$ Electrolyte Solution. *J. Power Sources* **2008**, *175*, 686−691.

(16) He, S.; Chen, W. 3D Graphene Nanomaterials for Binder-Free Supercapacitors: Scientific Design for Enhanced Performance. *Nanoscale* **2015**, *7*, 6957−6990.

(17) Xu, Y.; Lin, Z.; Huang, X.; Liu, Y.; Huang, Y.; Duan, X. Flexible Solid-State Supercapacitors Based on Three-Dimensional Graphene Hydrogel Films. *ACS Nano* **2013**, *7*, 4042−4049.

(18) Wu, Z.-S.; Winter, A.; Chen, L.; Sun, Y.; Turchanin, A.; Feng, X.; Müllen, K. Three-Dimensional Nitrogen and Boron Co-doped Graphene for High-Performance All-Solid-State Supercapacitors. *Adv. Mater.* **2012**, *24*, 5130−5135.

(19) Wang, W.; Guo, S.; Penchev, M.; Ruiz, I.; Bozhilov, K. N.; Yan, D.; Ozkan, M.; Ozkan, C. S. Three Dimensional Few Layer Graphene and Carbon Nanotube Foam Architectures for High Fidelity Supercapacitors. *Nano Energy* **2013**, *2*, 294−303.

(20) Choi, B. G.; Yang, M.; Hong, W. H.; Choi, J. W.; Huh, Y. S. 3D Macroporous Graphene Framworks for Supercapacitors with High Energy and Power Densities. *ACS Nano* **2012**, *6*, 4020−4028.

(21) Kitchen, H. J.; Vallance, S. R.; Kennedy, J. L.; Tapia-Ruiz, N.; Carassiti, L.; Harrison, A.; Whittaker, A. G.; Drysdale, T. D.; Kingman, S. W.; Gregory, D. H. Modern Microwave Methods in Solid-State Inorganic Materials Chemistry: From Fundamentals to Manufacturing. *Chem. Rev.* **2014**, *114*, 1170−1206.

(22) Tryba, A.; Morawski, A. W.; Inagaki, M. Preparation of Exfoliated Graphite by Microwave Irradiation. *Carbon* **2005**, *43*, 2417−2419.

(23) Sridhar, V.; Jeon, J.-H; Oh, I.-K. Synthesis of Graphene Nano-Sheets Using Eco-Friendly Chemical and Microwave Radiation. *Carbon* **2010**, *48*, 2953−2957.

(24) Shen, J.; Li, T.; Long, Y.; Shi, M.; Li, N.; Ye, M. One-step Solid State Preparation of Reduced Graphene Oxide. *Carbon* **2012**, *50*, 2134−2140.

(25) Zhu, Y.; Murali, S.; Stoller, M. D.; Velamakanni, A.; Piner, R. D.; Ruoff, R. S. Microwave Assisted Exfoliation and Reduction of Graphite Oxide for Ultracapacitors. *Carbon* **2010**, *48*, 2118−2122.

(26) Hu, H.; Zhao, Z.; Zhou, Q.; Gogotsi, Y.; Qiu, J. The Role of Microwave Absorption of Formation of Graphene from Graphite Oxide. *Carbon* **2012**, *50*, 3267−3273.

(27) Vadahanambi, S.; Jung, J.-H.; Oh, I.-K. Microwave Synthesis of Graphene and Graphene Decorated with Metal Nanoparticles. *Carbon* **2011**, *49*, 4449−4457.

(28) Lin, Y.; Baggett, D. W.; Kim, J.-W.; Siochi, E. J.; Connell, J. W. Instantaneous Formation of Metal and Metal Oxide Nanoparticles on Carbon Nanotubes and Graphene via Solvent-Free Microwave Heating. *ACS Appl. Mater. Interfaces* **2011**, *3*, 1652−1664.

(29) Hummers, W. S.; Offeman, R. E. Preparation of Graphitic Oxide. *J. Am. Chem. Soc.* **1958**, *80*, 1339.

(30) Niu, Z.; Chen, J.; Hng, H. H.; Ma, J.; Chen, X. A Leavening Strategy to Prepare Reduced Graphene Oxide Foams. *Adv. Mater.* **2012**, *24*, 4144−4150.

(31) Wang, G.; Ling, Y.; Wheeler, D. A.; George, K. E. N.; Horsley, K.; Heske, C.; Zhang, J. Z.; Li, Y. Facile Synthesis of Highly Photoactive $\alpha$-$Fe_2O_3$-Based Films for Water Oxidation. *Nano Lett.* **2011**, *11*, 3503−3509.

(32) Yu, H.; Fan, L.; Wu, J.; Lin, Y.; Huang, M.; Lin, J.; Lan, Z. Redox-Active Alkaline Electrolyte for Carbon-Based Supercapacitor with Pseudocapacitive Performance and Excellent Cyclability. *RSC Adv.* **2012**, *2*, 6736−6740.




DOI: 10.1021/acsami.5b06187
*ACS Appl. Mater. Interfaces* 2015, 7, 22364−22371

(33) Taberna, P. L.; Simon, P.; Fauvarque, J. F. Electrochemical Characteristics and Impedance Spectroscopy Studies of Carbon-Carbon Supercapacitors. *J. Electrochem. Soc.* **2003**, *150*, A292−A300.
(34) Basnayaka, P. A.; Ram, M. K.; Stefanakos, E. K.; Kumar, A. Supercapacitors Based on Graphene−Polyaniline Derivative Nanocomposite Electrode Materials. *Electrochim. Acta* **2013**, *92*, 376−382.
(35) Abdulhakeem, B.; Farshad, B.; Damilola, M.; Fatemeh, T.; Mopeli, M.; Julien, D.; Ncholu, M. Morphological Characterization and Impedance Spectroscopy Study of Porous 3D Carbons Based on Graphene Foam-PVA/Phenol-Formaldehyde Resin Composite as an Electrode Material for Supercapacitors. *RSC Adv.* **2014**, *4*, 39066−39072.
(36) Yang, T.; Lu, B. Highly Porous Structure Strategy to Improve the $SnO_2$ Electrode Performance for Lithium-Ion Batteries. *Phys. Chem. Chem. Phys.* **2014**, *16*, 4115−4121.
(37) Zhu, J.; Xu, Z.; Lu, B. Ultrafine Au Nanoparticles Decorated $NiCo_2O_4$ Nanotubes as Anode Material for High-Performance Supercapacitor and Lithium-Ion Battery Applications. *Nano Energy* **2014**, *7*, 114−123.
(38) Chen, Y.; Zhu, J.; Qu, B.; Lu, B.; Xu, Z. Graphene Improving Lithium-Ion Battery Performance by Construction of $NiCo_2O_4$/Graphene Hybrid Nanosheet Arrays. *Nano Energy* **2014**, *3*, 88−94.
(39) Shanmugavani, A.; Selvan, R. K. Synthesis of $ZnFe_2O_4$ Nanoparticles and Their Asymmetric Configuration with $Ni(OH)_2$ for a Pseudocapacitor. *RSC Adv.* **2014**, *4*, 27022−27029.
(40) Ma, W.; Nan, H.; Gu, Z.; Geng, B.; Zhang, X. Superior Performance Asymmetric Supercapacitors Based on $ZnCo_2O_4$@$MnO_2$ Core−Shell Electrode. *J. Mater. Chem. A* **2015**, *3*, 5442−5448.
(41) Gao, H.; Xiao, F.; Ching, C. B.; Duan, H. High-Performance Asymmetric Supercapacitor Based on Graphene Hydrogel and Nanostructured $MnO_2$. *ACS Appl. Mater. Interfaces* **2012**, *4*, 2801−2810.
(42) Qu, Q.; Zhang, P.; Wang, B.; Chen, Y.; Tian, S.; Wu, Y.; Holze, R. Electrochemical Performance of $MnO_2$ Nanorods in Neutral Aqueous Electrolytes as a Cathode for Asymmetric Supercapacitors. *J. Phys. Chem. C* **2009**, *113*, 14020−14027.


DOI: 10.1021/acsami.5b06187
*ACS Appl. Mater. Interfaces* 2015, 7, 22364−22371